X-Ray and Gamma-Ray Emission from the PSR 1259-63 / Be Star System

Hideki MAKI, Kenji MURATA,
Hidenori TAMAKI and Noriaki SHIBAZAKI

Department of Physics, Rikkyo University,
Nishi-Ikebukuro, Tokyo 171-8501

Abstract

PSR 1259-63 is a radio pulsar orbiting a Be star in a highly eccentric orbit. Soft and hard X-rays are observed from this unique system. We apply the shock powered emission model to this system. The collision of the pulsar and Be star winds forms a shock, which accelerates electrons and positrons to the relativistic energies. We derive the energy distribution of relativistic particles as a function of the distance from the shock in the pulsar nebula. We calculate the X-rays and γ-rays emitted from the relativistic particles in the nebula at various orbital phases, taking into account the Klein-Nishina effect fully. The shock powered emission model can explain the observed X-ray properties approximately. We obtain from the comparison with observations that a fraction of ~ 0.1 of the pulsar wind energy should be transformed into the final energy of non-thermal relativistic particles. We find that the magnetization parameter of the pulsar wind, the ratio of the Poynting flux to the kinetic energy flux, is ~ 0.1 and may decrease with distance from the pulsar. We predict the flux of 10 MeV-100 GeV γ-rays which may be nearly equal to the detection threshold in the future projects.

2

1. Observations

PSR 1259-63 is a 48 ms radio pulsar orbiting a Be star in a 3.4 yr orbit with eccentricity of 0.86 (Johnston et al. 1992a; Manchester et al 1995). The binary companion is a 10th magnitude B2e star SS 2883, whose mass and radius are estimated to be $\sim 10 M_\odot$ and $\sim 6\text{-}10 R_\odot$, respectively (Johnston et al. 1992b). The distance may be ~ 2 kpc (Taylor & Cordes 1993; Johnston et al. 1994).

The soft and hard X-rays observed from the PSR B1259-63/SS 2883 system have the following characteristics (Hirayama et al. 1999) : (1) the X-ray spectra are represented by a power law function that extends from 1 to 200 keV; (2) the spectral index varies with orbital phase, from ~ 2 at periastron to ~ 1.6 at apastron; (3) the X-ray luminosity in the 1-10 keV band varies with orbital phase by about an order of magnitude, from $\sim 10^{34}$ ergs/s near periastron to $\sim 10^{33}$ ergs/s at apastron, while just at periastron the light curve displays a drop by a factor of two compared to that slightly before or after the periastron; (4) the pulsation is absent in the X-ray time series. Only upper limits are reported for the high energy γ-ray emission above 1 MeV including TeV γ-rays (Tavani et al. 1996; Kawachi et al. 2002).

2. Shock Powered Emission Model

Tavani, Arons & Kaspi (1994), Tavani and Arons (1997) and Kirk, Ball & Skjaeraasen (1999) developed the shock powered emission model for the high energy emission from the PSR 1259-63 / SS 2883 system. The pulsar wind collides with the stellar wind ejected from the Be star, forming a shock. The shock accelerates the pulsar wind particles, electrons and positrons, to the relativistic high energies (Hoshino et al. 1992; Hoshino & Shimada 2002). The relativistic electrons and positrons in the nebula radiate keV-MeV photons through the synchrotron emission and GeV-TeV photons through the inverse Compton scattering of the photons from the Be star.
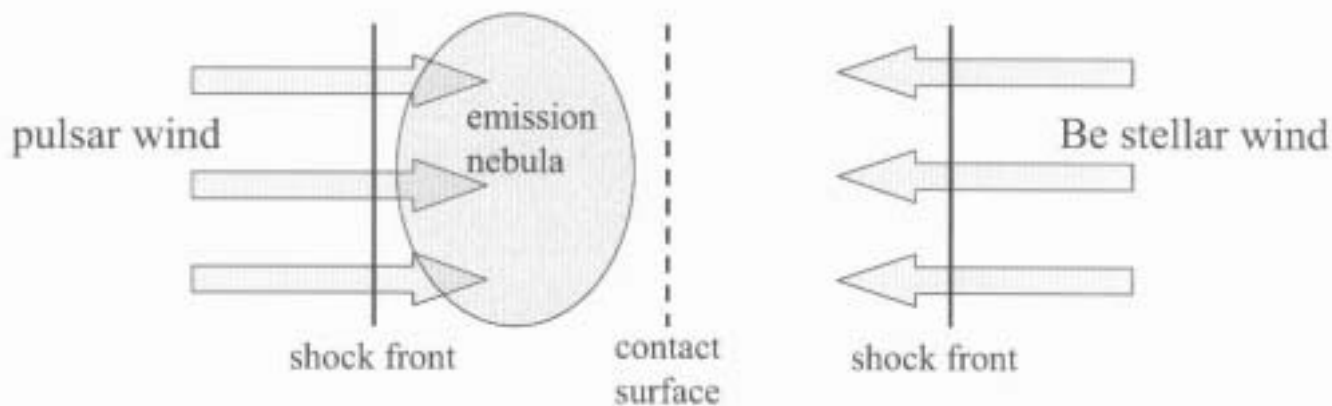
Fig. 1. Schematic diagram of the shock powered emission model.

We calculate the X-rays and γ-rays emitted from the shock accelerated particles at various orbital phases, taking into account the Klein-Nishina effect and the distributions for the target and scattered photons. Comparing with observations, we determine three important parameters involved in the model. Those are the fraction ε_a of the pulsar wind energy transformed into the final energy of non-thermal relativistic particles, the magnetization parameter σ, defined by the ratio of the Poynting flux to the kinetic energy flux in the pulsar wind, and the ratio ξ of the shock distance from the neutron star to the binary separation.

5

3. Cooling Times

Relativistic particles (electrons and positrons) lose energy through the synchrotron and inverse Compton processes, emitting X-rays and γ-rays, as they flow along the stream line in the postshock region. Relativistic particles may also suffer from the adiabatic energy loss. Here we estimate the cooling times of the relativistic particles using the physical parameters at the shock.
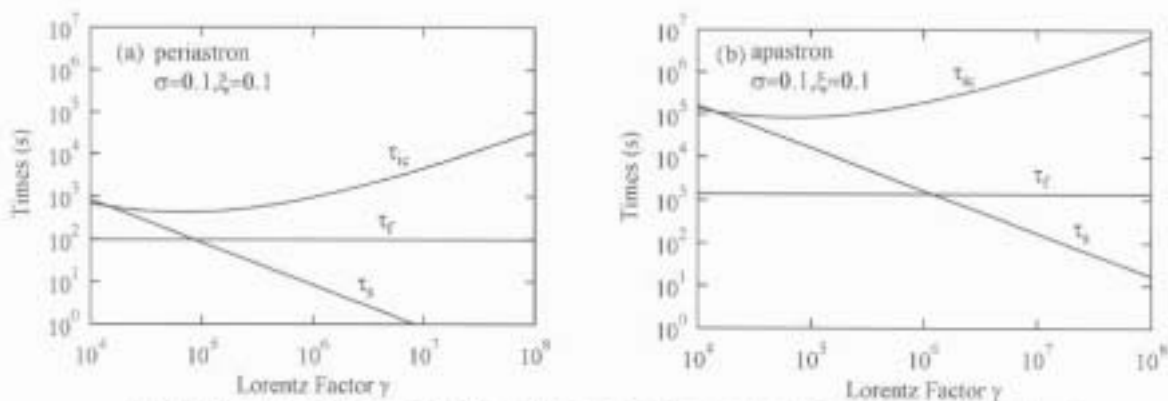

Fig. 2. Cooling and flow times of relativistic electrons and positrons at periastron (a) and apastron (b) plotted against the Lorentz factor. τ_s, τ_{ic} and τ_f express the synchrotron cooling time, the inverse Compton cooling time and the flow time, respectively. The model parameters used are $\sigma=0.1$ and $\xi=0.1$. The synchrotron cooling dominates over the inverse Compton cooling. The increase of τ_{ic} for larger γ reflects the Klein-Nishina effect.

6

We illustrate the cooling times at the periastron and apastron as a function of the Lorentz factor of relativistic particles in figure 2. The binary separations at periastron and apastron are $a=9.9\times10^{12}$ cm and $a=1.4\times10^{14}$ cm, respectively (Manchester et al 1995). We adopt $R_B\sim11R_\odot$ and $T\sim2.7\times10^4$ for the radius and effective surface temperature of the Be star (Johnston et al. 1992b). The physical parameters σ and ξ are chosen as $\sigma=0.1$ and $\xi=0.1$. The field strengths at the shock are $B_2\sim9.6$ G and $B_2\sim0.67$ G for periastron (figure 2a) and apastron (figure 2b), respectively. The synchrotron cooling time decreases simply with increasing Lorentz factor. On the other hand, the inverse Compton cooling time first decreases and then increases with increasing Lorentz factor. This behavior is a consequence of the Klein-Nishina effect that the inverse Compton scattering becomes less efficient at higher energies. The synchrotron emission dominates over the inverse Compton scattering at both periastron and apastron for $\gamma\gtrsim10^5$, which approximately corresponds to synchrotron emission in the X-ray band. Both the synchrotron and inverse Compton cooling times are longer at apastron than at periastron since the field strength and photon energy density are lower at apastron. Note that the synchrotron cooling time becomes shorter than the flow time at $\gamma>\gamma_b\sim10^5$ and at $\gamma>\gamma_b\sim10^6$ in figure 2a and figure 2b, respectively. As shown in section 4, there appears a break-off in the slope of the particle distribution and emission spectrum at the energy corresponding to γ_b since higher energy particles are lost rapidly.

4. Nebula Emission

We assume the non-thermal relativistic electrons and positrons of a power law distribution are injected at the shock. Then, these relativistic particles flow away from the shock, radiating X-rays and γ-rays. The particle distribution varies along a stream line. An emission nebula is formed in the shock down stream. The geometry of the emission nebula depends on the properties of the pulsar and Be star winds. Here, for simplicity, we approximate the nebula geometry by a cylinder with the length of $L\sim r_s$. The accelerated particles as well as the shocked pulsar wind flow through the cylinder, keeping the density constant. Hence, we ignore the adiabatic energy loss.

4.1 Distribution of Non-Thermal Relativistic Electrons and Positrons

We characterize the input particle distribution by the power law exponent p and the minimum and maximum Lorentz factors γ_1 and γ_2. We calculate the evolution of the particle distribution in the nebula, solving the integro-differential equation. We integrate the non-thermal relativistic particles over an entire emission nebula and then divide the integrated one by the nebula volume. We obtain the average energy distribution for the relativistic particles in the nebula, which we show in figure 3. As expected from figure 2, we observe that the slope of the particle distribution steepens by one, compared to the input particle distribution, above $\gamma_b \sim 10^5$ and $\gamma_b \sim 10^6$, where the synchrotron cooling time becomes equal to the flow time (figure 2), in the periastron and apastron cases, respectively.
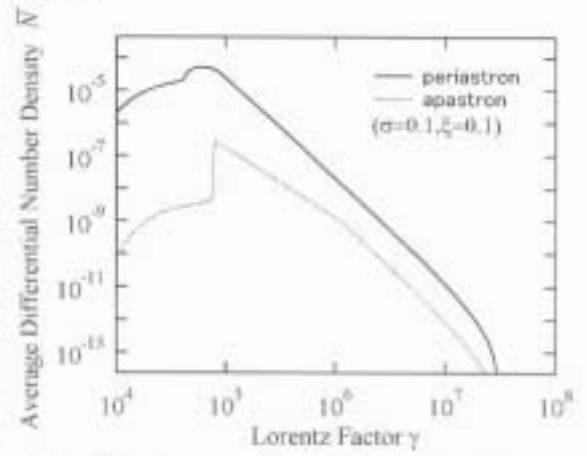

Fig. 3. Average distributions of relativistic electrons and positrons in the nebula at periastron (solid line) and at apastron (dotted line). The model parameters used are the same as those in figure 2. The synchrotron cooling is dominant over the inverse Compton cooling. The slope of the particle distribution steepens by one, compared to the input particle distribution, above $\gamma_b \sim 10^5$ and $\gamma_b \sim 10^6$, where the synchrotron cooling time becomes equal to the flow time (figure 2), respectively for the periastron and apastron cases.

9

Next, let us consider the average energy distribution of relativistic electrons and positrons when the energy loss of particles is determined mainly by the inverse Compton process. Choosing as $\sigma = 0.001$ and $\xi = 0.5$, we plot the average distribution at periastron in figure 4. In the solid line we include both the inverse Compton and synchrotron cooling although the inverse Compton cooling is far dominant over the synchrotron cooling. In the dotted line we retain only the synchrotron cooling, suppressing the inverse Compton cooling completely, in order to understand the effect of the inverse Compton process on the particle distribution. We observe in the solid line the flattening rather than steepening for the slope of the particle distribution at $\gamma > 10^5$, contrary to the synchrotron dominant case in figure 3. This flattening is caused by the Klein-Nishina effect. As seen from figure 2, the inverse Compton cooling is most efficient at $\gamma \sim 10^5$ and then becomes less efficient at $\gamma > 10^5$ because of the Klein-Nishina effect. The increase of the cooling time with increasing γ yields the flattening in the particle distribution.
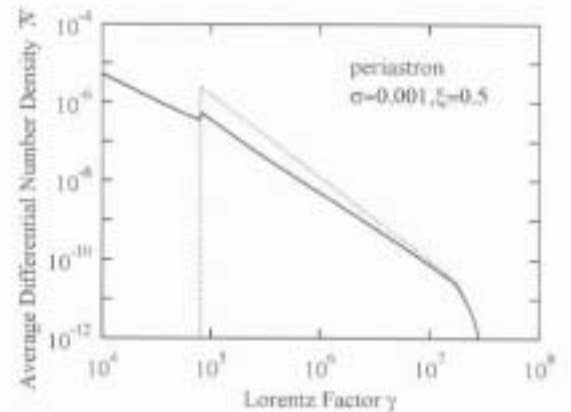

Fig. 4. Average distribution of relativistic particles at periastron for the case with $\sigma = 0.001$ and $\xi = 0.5$. The inverse Compton cooling is dominant over the synchrotron cooling. In the solid line both the Inverse Compton and synchrotron cooling are included, while in the dotted line the inverse Compton cooling is suppressed completely. The inverse Compton cooling causes fattening in the slope of the particle distribution.

10

4.2 Radiation Spectrum

The relativistic electrons and positrons in the nebula radiate keV-MeV photons through the synchrotron process and GeV-TeV photons through the inverse Compton process. We calculate the spectrum of X-rays and γ-rays radiated from the whole nebula, taking fully into account the particle distribution, the Klein-Nishina effect, the Planck distribution for the target photons of the inverse Compton scattering and the spectral function for synchrotron emission. We illustrate the X-ray and γ-ray spectra expected at periastron and apastron in figure 5, where we adopt the same particle distribution and physical parameters as those used in figure 3.
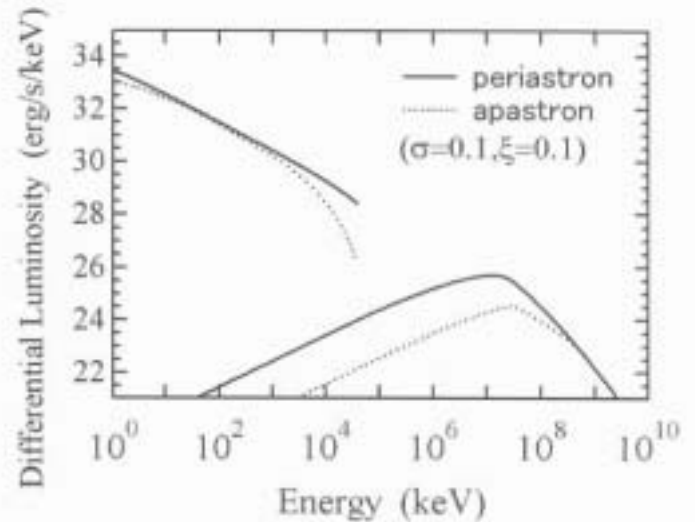

Fig. 5. Spectra of nebula emission at periastron (solid line) and apastron (dotted line). KeV-MeV photons are emitted by the synchrotron process, while GeV-TeV photons by the inverse Compton process. The model parameters used are the same as those in figure 3.

The spectral shape in the X-ray band is well represented by a power law function with exponents of ~1 and ~0.7 at periastron and apastron, respectively. The steeper gradient at periastron is a direct consequence of a steeper particle distribution at periastron, caused by the efficient synchrotron cooling. The X-ray luminosity decreases slightly with the binary separation. If we adopt the larger values for the maximum Lorentz factor γ_2, the spectrum of the synchrotron component extends to higher energies. Hence, if the sensitivity of observations in the 10 MeV - 1 GeV band is improved in future, the maximum Lorentz factor γ_2 of the particle acceleration would be determined.

The inverse Compton component peaks at a γ-ray energy of $\sim 10^{10}$ eV, as expected from the Lorenz factor at the peak of the particle distribution. Hence, the minimum of the input Lorenz factor, which may lie near the peak of the particle distribution, can be estimated from the observed γ-ray energy at the peak. The peak height of the inverse Compton component falls significantly with the binary separation because the density of target photons decreases and hence the inverse Compton scattering becomes less frequent as the binary separation enlarges. The spectral curves, as seen from the periastron and apastron cases, converge and become independent of the binary separation near the highest end of γ-ray energies. We should note that the number of ultrarelativistic particles responsible for these high energy γ-rays is determined by the synchrotron process and hence is inversely proportional to the energy density of the magnetic field whereas the inverse Compton scattering rate is proportional to the energy density of target photons. These two effects, when combined, cancel the dependence of the spectral curve on the shock distance and hence on the binary separation.

If the magnetic field at the shock is weak and the inverse Compton cooling dominates the synchrotron cooling, a larger number of relativistic electrons and positrons is required to produce such X-ray luminosity as shown in figure 5. Then, the GeV-TeV γ-ray luminosity is enhanced considerably compared to that in figure 5 (Kirk et al. 1998).

13

5. Comparison with Observations

We plot the photon spectral gradient (index) calculated at 5 keV for various model parameters as a function of the binary separation (a) in figure 6. The shock positions in figures 6b and 6c are taken to be 3 and 5 times farther away from the pulsar, respectively, compared to that in figure 6a. The magnetic field strengths at the shock are larger for larger σ and smaller a and ξ, while the target photon densities are larger for larger ξ and smaller a. We assume that the distributions of accelerated particles at the shock are the same irrespective of the binary phase. We fix the minimum and maximum Lorentz factors for the input particle distribution to $\gamma_1 \sim 8 \times 10^4$ and $\gamma_2 \sim 3 \times 10^7$, respectively. The change of the particle distribution in the nebula due to the radiative cooling is not significant at apastron. Hence, the photon spectral index at apastron reflects the original slope of the accelerated particle distribution. We adopt $p \sim 2.1$ determined from the photon index of ~ 1.6 observed at apastron. The observed photon index variation with orbital phase is approximately reproduced by the case with $\sigma \sim 0.1$ and $\xi \sim 0.1$ in figure 6a. Contrary to the results in figure 11 of Tavani and Arons (1997), we find that the efficient synchrotron cooling is responsible for the spectral steepening in the X-ray band around periastron. As clearly seen at periastron for $\sigma \sim 0.001$ in figure 4, if the inverse Compton cooling dominates, the spectral slope rather flattens because of the Klein-Nishina effect. If the Klein-Nishina effect is fully taken into account, some results of Tavani and Arons (1997) may be altered.
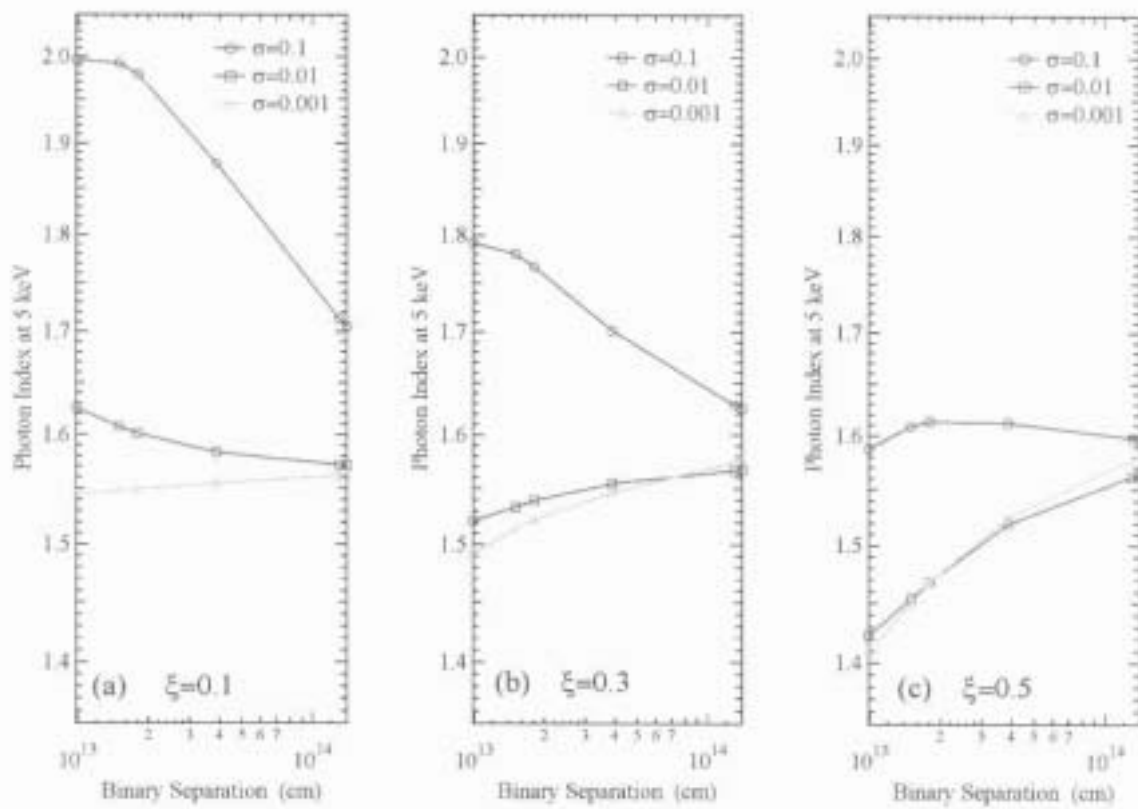
14

Fig. 6. Photon spectral indices calculated at 5 keV for various model parameters as a function of the binary separation. For larger σ and smaller ξ the synchrotron emission dominates over the inverse Compton scattering, leading to the spectral steepening. For smaller σ and larger ξ, on the other hand, the inverse Compton scattering dominates over the synchrotron emission, leading to the spectral flattening.

15

We depict the X-ray luminosity in the 1-10 keV band calculated for various model parameters as a function of the binary separation in figure 7. The case with $\xi \sim 0.1$ and $\sigma \sim 0.1$ is again preferred from the relatively large observed X-ray luminosity. However, if the model parameters ξ and σ are taken to be constant throughout the binary orbit, the luminosity variation with orbital separation predicted by the model is too small to explain the observed variation amounting to an order of magnitude. This result suggests that the magnetization parameter σ may decrease with orbital separation while the shock position parameter ξ may increase with orbital separation.

The magnetization parameter is likely to decrease with distance from the neutron star in the pulsar wind. Note that the small value of $\sigma \sim 0.003$ is reported for the Crab pulsar wind from the nebula analysis (Kennel and Coroniti 1984). In the Crab pulsar the distance of the shock, where the magnetization parameter is diagnosed, from the neutron star is ~ 0.1 pc, while in the PSR B1259-63 $\sim 10^{12} - 10^{13}$ cm. When combined with our result of the PSR B1259-63, the result of the Crab pulsar strengthens the conclusion that the magnetization parameter may decrease with distance from the neutron star. The magnetization parameter and shock distance presented here can be used to study the property of a pulsar wind.
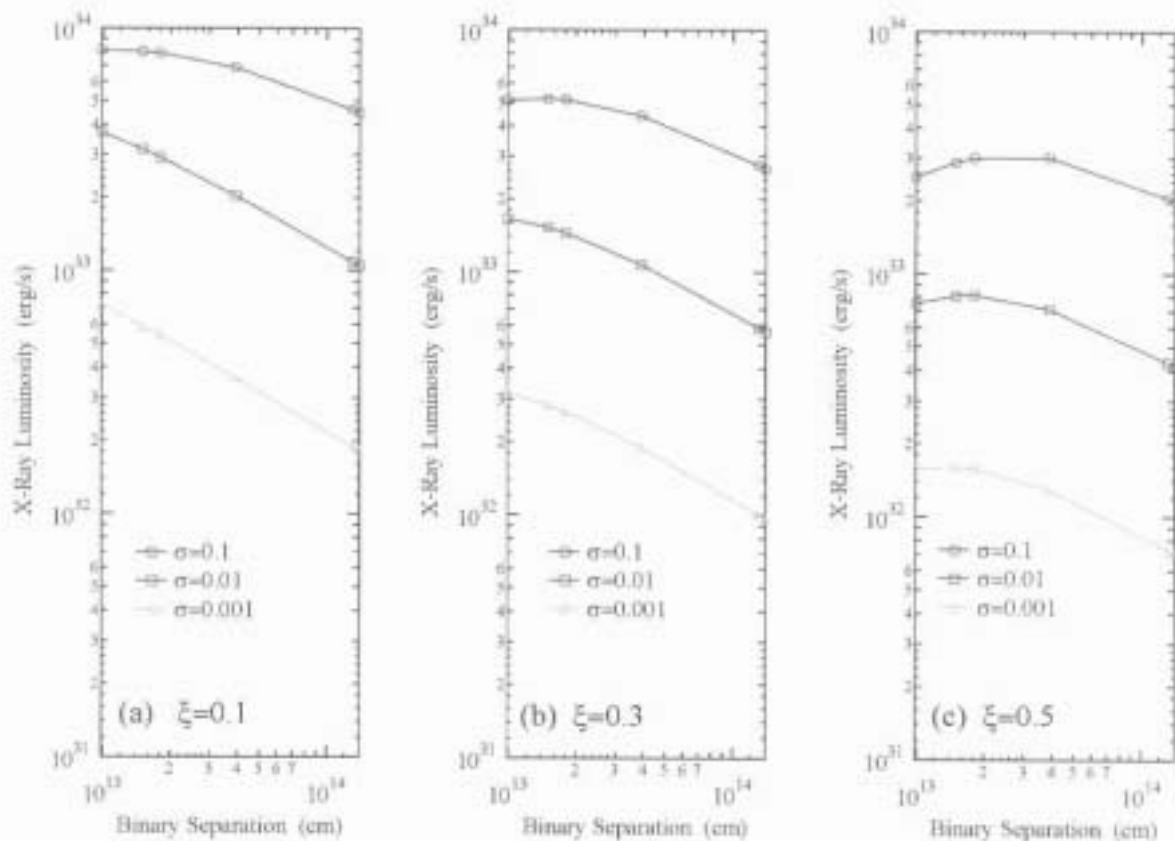
16

Fig. 7. Luminosity of X-rays in the 1-10 keV band calculated for various model parameters as a function of the orbital separation. X-ray photons are emitted by the synchrotron process. The magnetic field strength in the nebula and hence the synchrotron emission rate decrease with decreasing σ.

Our results shown in figure 5 are consistent with the COMPTEL and EGRET upper limits in the 1-1000 MeV range. Recently, the CANGAROO collaboration reports the new upper limit on the emission in the TeV range (Kawachi et al. 2002), which is well above our prediction and consistent with our results. Note, however, that the reproduction of a luminosity drop in X-rays, observed just at periastron, is beyond the scope of our simple model. We need to construct the detailed model that includes the flow patterns of the Be star and pulsar winds, the misalignment of the pulsar orbital plane with the Be star outflow disk, the shielding of the emission region from the target photons for the inverse Compton scattering and the adiabatic loss in addition to the variation of model parameters σ and ξ with orbital separation.

6. Concluding Remarks

The PSR 1259–63 / Be star system can provide important information on the pulsar wind. We can diagnose the property of the pulsar wind at various distances from the pulsar by applying the shock powered emission model to the X-ray fluxes and spectra observed at different orbital phases because the binary orbit is highly eccentric. We find that the magnetization parameter of the pulsar wind, the ratio of the Poynting flux to the kinetic energy flux, is ~0.1 at the distance of ~10^{12} cm and may decrease with distance from the pulsar. Note that the magnetization parameter of the Crab pulsar wind is ~0.003 at the distance of ~0.1 pc. These two results, when combined, strengthen our conclusion that the magnetization parameter may decrease with distance from the neutron star. We need more X-ray data from various pulsar nebulae in order to determine the pulsar wind property as a function of distance from the pulsar and to understand the energy conversion from the Poynting flux to the kinetic energy flux in the pulsar wind.

The PSR 1259–63 / Be star system can also provide valuable information on the shock acceleration. We find that a fraction of ~ 0.1 of the pulsar energy is transformed into the final energy of non-thermal relativistic electrons and positrons. We obtain the power law index of ~2 for the distribution of the shock accelerated particles. We should note that the maximum energy of accelerated particles can be estimated from the break-off energy in the photon spectrum. We expect this spectral break in the MeV-GeV range, which may be detectable by the future program GLAST. We may derive the minimum energy of shock accelerated particles from the high energy γ-rays due to the inverse Compton emission. The observations of GeV-TeV γ-rays are also encouraged.

References

Blumenthal, G. R. 1970, Rev. Mod. Phys., 42, 237

Cominsky, L., Roberts, M., & Johnston, S. 1994, ApJ, 427, 978

Greiner, J., Tavani, M., & Belloni, T. 1995, ApJ, 441, L43

Grove, J. E., Tavani, M., Purcell, W. R., Johnston, W. N., Kurfess, J. D., Strickman, M. S., & Arons, J. 1995, ApJ, 447, L43

Hirayama, M., Nagase, F., Tavani, M., Kaspi, V. M., Kawai, N., & Arons, J. 1996, PASJ, 48, 833

Hirayama, M., Cominsky, L. R., Kaspi, V. M., Nagase, F., Tavani, M., Kawai, N. & Grove, J. E. 1999, ApJ, 521, 718

Hoshino, M., Arons, J., Gallant, Y. A., & Langdon, A. B. 1992, ApJ, 390, 454

Hoshino, M., & Shimada, N. 2002, ApJ, 572, 880

Johnston, S., Lyne, A. G., Manchester, R. N., Kniffen, D. A., D'Amico, N., Lim, J., & Ashworth, M. 1992a, MNRAS, 255, 401

Johnston, S., Manchester, R. N., Lyne, A. G., Bailes, M., Kaspi, V. M., Guojun, Q., & D'Amico, N. 1992b, ApJ, 387, L37

Johnston, S., Manchester, R. N., Lyne, A. G., Nicastro, L., & Spyromilio, J. 1994, MNRAS, 268, 430

Jones, F. C. 1968, Phys. Rev., 167, 1159

Kaspi, V. M., Tavani, M., Nagase, F., Hirayama, M., Hoshino, M., Aoki, T., Kawai, N., & Arons, J. 1995, ApJ, 453, 424

Kawachi et al. 2002, preprint

Kennel, C. F., & Coroniti, F. V. 1984, ApJ, 283, 694

Kirk, J. G., Ball, L., & Skjaeraasen, O. 1999, Astroparticle Physics, 10, 31

Manchester, R. N., Johnston, S., Lyne, A. G., D'Amico, N., Bailes, M., & Nicastro, L. 1995, ApJ, 445, L137

Tavani, M., Arons, J., & Kaspi, V. M. 1994, ApJ, 433, L37

Tavani, M., Grove, J. E., Purcell, W., Hermsen, W., Kuiper, L., Kaaret, P., Ford, E., Wilson, R. B., Finger, M., Harmon, B. A., Zhang, S. N., Mattox, J., Thompson, D., & Arons, J. 1996, A&AS, 120, 221

Tavani, M., & Arons, J. 1997, ApJ, 477, 439

Taylor, J. H., & Cordes, J. M. 1993, ApJ, 411, 674